



1 Influence of the sudden stratosphere warming on quasi-2 day waves

2 Sheng-Yang Gu^{1, 2, 3*}, Han-Li Liu⁴, Xiankang Dou^{1, 3}, Tao Li^{1, 3}

3

4 ¹CAS Key Laboratory of Geospace Environment, Department of Geophysics and

5 Planetary Science, University of Science and Technology of China, Hefei, Anhui,

6 China

7 ²Key Laboratory of Earth and Planetary Physics, Institute of Geology and Geophysics,

8 Chinese Academy of Sciences

9 ³Mengcheng National Geophysical Observatory, School of Earth and Space Sciences,

10 University of Science and Technology of China, Hefei, Anhui, China

11 ⁴High Altitude Observatory, National Center for Atmospheric Research, Boulder,

12 Colorado, USA

13

14

15 *Corresponding author: S.-Y. Gu, CAS Key Laboratory of Geospace Environment,

16 School of Earth and Space Science, University of Science and Technology of China,

17 96 Jin-zhai Rd, Hefei, Anhui 230026, China. (gsy@ustc.edu.cn).



18 **Abstract:**

19 The influence of the sudden stratosphere warming (SSW) on quasi-2 day wave
20 (QTDW) with westward zonal wavenumber 3 (W3) is investigated using the
21 Thermosphere-Ionosphere-Mesosphere-Electrodynamics General Circulation Model
22 (TIME-GCM). The summer easterly jet below 90 km is strengthened during an SSW,
23 which results in a larger refractive index and thus more favorable condition for the
24 propagation of W3. In the winter hemisphere, the Eliassen Palm (EP) flux diagnostics
25 indicate that the strong instabilities at middle and high latitudes in the mesopause
26 region are important for the amplification of W3, which are weakened during SSW
27 periods due to the deceleration or even reversal of the winter westerly winds.
28 Nonlinear interactions between the W3 and the wavenumber 1 stationary planetary
29 wave produce QTDW with westward zonal wavenumber 2 (W2). The meridional
30 wind perturbations of the W2 peak in the equatorial region, while the zonal wind and
31 temperature components maximize at middle latitudes. The EP flux diagnostics
32 indicate that the W2 is capable of propagating upward in both winter and summer
33 hemispheres, whereas the propagation of W3 is mostly confined to the summer
34 hemisphere. This characteristic is likely due to the fact that the phase speed of W2 is
35 larger, and therefore its waveguide has a broader latitudinal extension. The larger
36 phase speed also makes W2 less vulnerable to dissipation and critical layer filtering
37 by the background wind when propagating upward.

38



39 1. Introduction

40 The westward quasi-2 day wave (QTDW) is a predominant phenomenon in the
41 mesosphere and lower thermosphere (MLT) region in the summer hemisphere with
42 zonal wavenumbers 2, 3, and 4. The QTDW was observed by the neutral temperature
43 measurements from Upper Atmosphere Research Satellite (UARS) [Wu *et al.*, 1996],
44 Aura satellite [Tunbridge *et al.*, 2011] and Thermosphere Ionosphere and Mesosphere
45 Electric Dynamics (TIMED) satellite [Gu *et al.*, 2013a], and the neutral wind
46 measurements from UARS High Resolution Doppler Imager (HRDI) [Wu *et al.*, 1993],
47 TIMED TIDI [Gu *et al.*, 2013a], and medium frequency radar [Gu *et al.*, 2013b]. In
48 addition, numerical simulations, including one-dimensional model [Plumb, 1983],
49 two-dimensional model [Rojas and Norton, 2007], three dimensional TIME-GCM
50 [Yue *et al.*, 2012] and the Navy Operational Global Atmospheric Prediction System
51 Advanced Level Physics, High Altitude (NOGAPS-ALPHA) forecast-assimilation
52 system [McCormack, 2009], have also been utilized to study the QTDW. Using
53 neutral temperature and horizontal wind observations from the TIMED satellite, Gu *et*
54 *al.* [2013a] showed that the QTDW with westward zonal wavenumber 3 (W3) is
55 amplified during January/February in the southern hemisphere, and that the QTDW
56 with westward zonal wavenumber 4 (W4) reaches a maximum amplitude during
57 July/August in the northern hemisphere. The amplitude of the W3 is nearly twice as
58 strong as the W4. It is proposed that the W3 is the Rossby-gravity mode (3, 0) [Salby,
59 1981], which can be modulated by the mean flow instabilities [Plumb, 1983;
60 Limpasuvan *et al.*, 2000; Salby and Callaghan, 2001; Yue *et al.*, 2012]. The W4 is



61 first reported by *Rodgers and Prata* [1981] in the radiance data from the Nimbus 6
62 satellite, which was also confirmed by *Plumb* [1983] with a one-dimensional model
63 under summer easterly conditions. Usually, the W4 is believed to be an unstable mode
64 induced by the summer easterly instabilities [*Plumb*, 1983; *Burks and Leovy*, 1986].
65 Compared with W3 and W4, there are much less reports on the QTDW with westward
66 zonal wavenumber 2 (W2).

67 *Tunbridge et al.* [2011] studied the zonal wavenumbers of the summer time
68 QTDW with satellite temperature observations from 2004 to 2009. They found that
69 the W2 is amplified mainly during January in the southern hemisphere with a
70 maximum amplitude at middle latitudes, which always coincides with the temporal
71 variations of the W3. The horizontal wind observations from the HRDI instrument
72 onboard the UARS satellite showed that the meridional wind perturbations of the W2
73 maximize in the equatorial region at the mesopause [*Riggin et al.*, 2004]. This W2
74 was suggested to be excited in-situ at high altitude, which has little direct connection
75 with the 2-day activities at lower altitudes. Anomalous 2-day wave activities with
76 zonal wavenumber 2 were also observed in the Aura/MLS temperature and
77 line-of-sight wind [*Limpasuvan and Wu*; 2009], which was suggested to be an
78 unstable mode induced by the strong summer easterly jet during January 2006. *Rojas*
79 *and Norton* [2007] found a wavenumber 2 westward propagating wave mode with a
80 period of 49 h in a linear two-dimensional model under boreal summer easterly
81 condition, which maximized at middle and high latitudes in the summer hemisphere
82 for both temperature and neutral wind components. The zonal wind and meridional



83 wind perturbations also exhibited a smaller peak at low latitudes in the winter
84 hemisphere and at the equator, respectively.

85 It is known that nonlinear interactions between planetary scale waves can
86 contribute to atmospheric variability. For example, TIMED/SABER temperature
87 observations during January 2005 showed that the nonlinear interactions between the
88 W3 and the migrating diurnal tide could produce an eastward QTDW with zonal
89 wavenumber 2 [Palo *et al.*, 2007]. The nonlinear interactions between the
90 quasi-stationary planetary waves (QSPW) and the migrating tides lead to changes in
91 tides, which then transmit the QSPW signals into the ionosphere at low and middle
92 latitudes through the E region wind dynamo [Liu *et al.*, 2010; Liu and Richmond,
93 2013]. Nevertheless, the nonlinear interactions between QTDW and other planetary
94 waves have not been reported.

95 Rapid growth of QSPWs and their forcing are believed to be the main drivers of
96 the sudden stratosphere warming (SSW) at high latitudes in the winter hemisphere
97 [Matsuno, 1971], which causes inter-hemispheric connections at different altitudes
98 [e.g. Karlsson *et al.*, 2007, 2009; Tan *et al.*, 2012]. The wave-mean flow interactions
99 could decelerate or even reverse the eastward winter stratosphere jet, which, in return,
100 prevents the further growth of the QSPW. The SSW in the northern hemisphere occurs
101 usually in January/February, accompanied with a strong zonal wavenumber 1 or 2
102 QSPW at high latitudes [Pancheva *et al.*, 2008; Harada *et al.*, 2009; Manney *et al.*,
103 2009; Funke *et al.*, 2010]. There have been recent studies suggesting possible
104 connection between QTDW and SSW [McCormick *et al.*, 2009; Chandran *et al.*,



2013]. However, it is not clear if this is because both QTDW and SSW tend to occur in mid to late January, or if the flow condition around SSW is more favorable for QTDW propagation and/or amplification. In this paper, we investigate the influence of SSW on QTDW using the National Center for Atmosphere Research (NCAR) TIME-GCM. The numerical experiments are described in section 2. Section 3 are the analysis results from the model simulations. Section 4 discusses the contributions of QTDW to the summer mesospheric polar warming. Our conclusions are presented in section 5.

2. Datasets and analysis

2.1 TIMED satellite observations

The Thermosphere Ionosphere and Mesosphere Electric Dynamics (TIMED) satellite was launched at the end of 2001, which focuses on the dynamics study of the mesosphere and lower thermosphere. The TIMED Doppler Imager (TIDI) instrument on board the TIMED satellite has been providing global horizontal wind observations since late January 2002. The NCAR-processed version 0307A of P9 line TIDI wind datasets are utilized here to investigate the inter-annual variations of the QTDWs during austral summer periods. The vertical resolution of the TIDI winds between 85 and 105 km is ~2 km, with the highest precision at ~95 km [Killeen *et al.*, 2006]. The version 0307A TIDI horizontal winds have been used in the study of mesospheric tidal variations and QTDWs [Wu *et al.*, 2008; Gu *et al.*, 2013]. A two-dimensional least square fitting method, which was provided by Gu *et al.* [2013a; 2015], is also adopted to extract the QTDW signals in this study.



127 **2.2 TIME-GCM simulations**

128 The NCAR TIME-GCM simulates the global atmosphere from the upper
129 stratosphere to the thermosphere, and the ionospheric electrodynamics [*Roble and*
130 *Ridley*, 1994; *Roble*, 2000; *Richmond et al.*, 1992], which is self consistent. The input
131 solar EUV and UV spectral fluxes are parameterized by the solar flux index at 10.7
132 cm wavelength (F10.7), and it is set to 150 sfu (solar flux unit) in our model
133 simulations. The auroral electron precipitation is parameterized by hemispheric power
134 [*Roble and Ridley*, 1987] and the ionospheric convection is driven by the
135 magnetosphere-ionosphere current system [*Heelis et al.*, 1982]. The hemispheric
136 power is set to 16 and the cross-cap potential is set to 60 in our simulations. The
137 gravity wave forcing is parameterized based on linear saturation theory [*Lindzen*,
138 1981]. Climatologic migrating tides from the Global Scale Wave Model (GSWM) are
139 specified at the lower boundary. The model is capable of simulating the upward
140 propagation of planetary waves by superimposing periodical geopotential height
141 perturbations at the lower boundary (~30 km). We use the regular horizontal
142 resolution of $5^{\circ} \times 5^{\circ}$ longitude and latitude grids in the current study. There are 49
143 pressure levels from 10 hPa (~30 km) to the upper boundary of 3.5×10^{-10} hPa (~550
144 km) with a vertical resolution of one-half scale height. The tides are generally weak
145 compared with climatology in this single version of TIME-GCM. But this does not
146 alter our conclusion with regard to 2-day waves.

147 To simulate the QTDW, geopotential height perturbations of 1000 m with
148 wavenumber 3 were forced at the TIME-GCM lower boundary. The Gaussian-shaped



149 geopotential height perturbations for W3 peaked at 30°N, extending from 10°S to
150 70°N. To simulate the SSW, geopotential height perturbations of 1000 and 2800 m for
151 a stationary planetary wave with zonal wavenumber 1 (SPW1) were specified at the
152 lower boundary for weak and strong warming, respectively. The Gaussian-shaped
153 geopotential height perturbations for SPW1 peaked at 60°N, extending from 35°N to
154 85°N. In fact, the European Centre for Medium-Range Weather Forecasts (ECMWF)
155 dataset during 2011/2012 austral summer period shows that both the geopotential
156 perturbations of the W3 and SPW1 maximize in the northern (winter) hemisphere at
157 the model lower boundary (not shown). The model was run under perpetual
158 conditions for 40 days with the calendar date set to January 20. Both the W3 and
159 SPW1 gained maximum amplitudes on day 10 with a Gaussian-shaped increase from
160 day 1 to 10. The forcing of W3 was reduced following the same Gaussian function
161 from days 25 to 40. The forcing of SPW1 was sustained from days 10 to 40. The
162 parameters for the control run (base case) and four different experimental runs (case 1,
163 2, 3, and 4) are summarized in Table 1. No W3 or SPW1 forcing was specified at the
164 TIME-GCM lower boundary in the base case, which ran for 15 days to equilibrate and
165 was utilized as initial conditions for the other experimental cases. Case 1 was a
166 standard run for W3 and only geopotential height perturbations of W3 were forced.
167 Case 2 and case 3 were designed to study the amplification of W3 under weak and
168 strong SSW conditions, respectively. The same W3 forcing was added in cases 2 and
169 3, whereas the SPW1 forcing was stronger in case 3 than that in case 2. Case 4 was a
170 standard run for SSW in which only the forcing of SPW1 was included.



171

172 **3. Observational results**

173 Figure 1 shows the ECMWF zonal mean temperature at 80N and 10 hPa from
174 December to February during 2003-2012. The strongest SSW occurred in January
175 2009, followed by the second strongest SSW in January 2006. Besides, the SSWs in
176 2012, 2004 and 2010 were also very strong. Figure 2 shows the temporal variations of
177 the wave number 3 QTDW in January and February during 2003-2012. The
178 amplitudes were averaged between 90 and 100 km. The W3 peaked regularly in late
179 January and early February every year but with strong inter-annual variabilities. For
180 example, the W3 reached minima in January of 2008 and 2009. It is also clear that the
181 W3 was strong during the strong SSW years of 2004, 2006 and 2012. Nevertheless,
182 the W3 was extremely weak during the strongest SSW year of 2009. Figure 3 shows
183 the averaged amplitudes of the wave number 2 QTDW between 90 and 100 km during
184 2003-2012, which also maximized in January and February. The W2 was the strongest
185 during the strong SSW year of 2006, followed by the W2 event in 2012. We can see
186 that the QTDWs could be very strong during some SSW years, but not during all the
187 SSW years. Our question is whether the SSW and QTDW (both W2 and W3) impact
188 each other, and this will be numerically studied in the following section.

189 **4. Simulation results and Discussion**

190 **4.1 Zonal mean background condition**

191 Since the model time was set perpetually on January 20, the background
192 temperature and zonal wind in our simulations should show typical northern



193 winter/southern summer conditions. Figures 4a and 4b show the zonal mean
194 temperature and zonal mean zonal wind on model day 28 (when W3 peaks) in case 1,
195 which only has W3 forcing. The zonal mean temperature in TIME-GCM shows a cold
196 summer mesopause and a warm winter mesopause. The zonal mean zonal wind is
197 westward in the summer mesosphere and eastward in the winter mesosphere. It is
198 clear that the global structures of the zonal mean temperature and zonal wind
199 generally agree with climatology from for example previous TIMED/SABER
200 temperature [Mertens *et al.*, 2009] and UARS/HRDI wind [Swinbank and Ortland,
201 2003] observations, as well as the NOGAPS-ALPHA forecast assimilations
202 [McCormack, 2009].

203 We then investigate the atmospheric responses to the weak and strong SSW event
204 in cases 2 and 3, respectively. Figures 4c and 4e show the temperature differences on
205 model day 28 between case 2 and case 1, and between case 3 and case 1, respectively.
206 In cases 1, 2 and 3, the same W3 forcing is specified at the lower boundary, whereas
207 SPW1 is only specified in cases 2 and 3. The SPW1 forcing in case 2 is weaker than
208 that in case 3. Compared with case 1, which does not have a stationary planetary wave
209 specified at the model lower boundary, the temperature of case 2 is warmer by 15-20
210 K below 60 km and is colder by 20-25 K between 60 and 110 km at high latitudes in
211 the winter hemisphere. Both the cooling and warming in case 3 are stronger than in
212 case 2 due to the stronger SPW1 in case 3. The warming and cooling in the
213 stratosphere and mesosphere for the strong SSW are ~40 K and ~60 K, respectively.
214 In addition, weaker warming is observed between 70 and 100 km in the middle and



low latitude regions and above 80 km at high latitudes in the summer hemisphere. The corresponding zonal mean zonal wind differences are shown in Figure 4d and 4f. The zonal mean zonal wind decreases by ~ 30 m/s and ~ 70 m/s in the winter stratosphere and lower mesosphere in the weak (case 2) and strong (case 3) SSW events, respectively. It increases by ~ 30 m/s and ~ 50 m/s in the mesopause region in the weak and strong SSW events, respectively. Generally, the SSW features in our simulations (e.g. the increasing temperature and decreasing westerly in the winter stratosphere high latitude region) agree with previous reports [Funke *et al.*, 2010; Yamashita *et al.*, 2010; Tan *et al.*, 2012].

4.2 The influences on W3

Figure 5a shows the wavenumber-period spectrum of the meridional wind during days 25-30 of case 1. The meridional wind at ~ 82 km and 7.5°S is utilized in the analysis. The westward wavenumber 3 QTDW dominates the whole spectrum, with negligible signatures at other wavenumbers and periods. The spectra of zonal wind and temperature show similar W3 signatures as the meridional wind (not shown). Figure 5b shows the latitudinal and vertical structure of the W3 in meridional wind, which maximizes at low latitudes in the southern hemisphere mesopause region with an amplitude of ~ 60 m/s. Shown in Figure 5c is the structure of the W3 in zonal wind, which peaks at middle and low latitudes in both hemispheres with maximum amplitude nearly half of the peak meridional wind amplitude. The zonal wind peak of ~ 30 m/s in the summer (southern) hemisphere is slightly larger than that of ~ 20 m/s in the winter hemisphere, most likely due to the additional amplification by the



237 baroclinic/barotropic instability of the summer easterly. Figure 5d shows the global
 238 structure of the W3 in temperature, which also peaks at middle latitudes. In the
 239 summer hemisphere, the temperature perturbations peak at ~105 km and ~80 km with
 240 amplitudes of ~7 K and ~8 K, respectively. In the winter hemisphere, the peak of the
 241 W3 at ~80 km is much weaker than that between 100 and 110 km. We should note
 242 that the rapid decay of W3 near the model lower boundary (~30 km) is an artifact near
 243 the model lower boundary. In all, the vertical and latitudinal structures of the 2-day
 244 wave in our simulations generally agree with the TIMED/SABER temperature and
 245 TIMED/TIDI observations [*Palo et al.*, 2007; *Gu et al.*, 2013].

246 Figure 6 shows the temporal variations of the W3 in meridional wind at ~82 km
 247 for case 1, case 2 and case 3. Note that the same perturbations for W3 were forced at
 248 the lower model boundary for all the three experimental runs. The W3 forcing was
 249 gradually increased from day 1 to 10, and was reduced after day 25 with constant
 250 amplitude between day 10 and 25. The perturbations of SPW1 in case 2 were nearly
 251 three times larger than case 3, both of which were sustained after day 10 with a
 252 Gaussian-shaped increase from day 1 to 10. The W3 in case 1 is the strongest with an
 253 amplitude of ~60 m/s (Figure 6a). The maximum amplitudes of the W3 in case 2 and
 254 case 3 are ~40 m/s and ~35 m/s (Figure 6b and 6c), respectively. It is evident that the
 255 amplitudes of the W3 are weakened during the SSW periods. In the following, we will
 256 examine possible causes of the QTDW decrease during SSW.

257 The refractive index m of a forced planetary wave is [*Andrews et al.*, 1987]:

$$258 \quad m^2 = \frac{\bar{q}_\phi}{a(u-c)} - \frac{s^2}{(a \cos \phi)^2} - \frac{f^2}{4N^2 H^2}, \quad (1)$$



where s , c , \bar{u} , a , φ , f , N , and H are the zonal wavenumber, phase speed, zonal mean
 zonal wind, earth radius, latitude, Coriolis parameter, Brunt-Väisälä frequency, and
 scale height, respectively. And \bar{q}_φ is the latitudinal gradient of the quasi-geostrophic
 potential vorticity:

$$\bar{q}_\varphi = 2\Omega \cos \varphi - \left(\frac{(\bar{u} \cos \varphi)_\varphi}{a \cos \varphi} \right)_\varphi - \frac{a}{\rho} \left(\frac{f^2}{N^2} \rho \bar{u}_z \right)_z, \quad (2)$$

where Ω is the angular speed of the earth's rotation, ρ is the background air density,
 and z means the vertical gradient. A necessary condition for baroclinic/barotropic
 instability is $\bar{q}_\varphi < 0$, and the planetary waves are propagating (evanescent) where m^2
 is positive (negative). Moreover, the meridional and vertical components (EPY and
 EPZ) of the Eliassen-Palm (EP) flux vector (F) for planetary waves can also be
 calculated with reconstructed wave perturbations from the TIME-GCM, defined
 following *Andrews et al.* [1987] as:

$$F = \begin{bmatrix} \text{EPY} \\ \text{EPZ} \end{bmatrix} = \rho a \cos \varphi \begin{bmatrix} \frac{\bar{u}_z \bar{v}' \bar{\theta}'}{\bar{\theta}_z} - \bar{v}' \bar{u}' \\ \left[f - \frac{(\bar{u} \cos \varphi)_\varphi}{a \cos \varphi} \right] \frac{\bar{v}' \bar{\theta}'}{\bar{\theta}_z} - \bar{w}' \bar{u}' \end{bmatrix} \quad (3)$$

Here u' , v' , w' and θ' are the QTDW perturbations in zonal wind,
 meridional wind, vertical wind and potential temperature, respectively.

First, we examine the baroclinic/barotropic instabilities, waveguide and the EP
 flux of the W3 for these cases. The averaged zonal mean zonal wind for case 1, case 2
 and case 3 during days 25-30, when the W3 reaches the maximum amplitude, are
 depicted by the black contour lines in Figures 7a, 7c and 7e, respectively.
 Over-plotted are the negative regions of \bar{q}_φ by blue shades, which is a prerequisite for



the occurrence of mean flow instability, and the positive regions of the waveguide for W3 by orange shades, which show where wave propagation is favorable. Shown in Figures 7b, 7d and 7f are the EP flux vectors (red arrows) of W3 and their divergences (light blue shades and dot lines) for case 1, case 2 and case 3, respectively. We will first compare results of case 1 (Figures 7a and 7b) with case 2 (Figures 7c and 7d). A region of negative \bar{q}_ϕ is seen in case 1 between 80 and 100 km at middle and high latitudes in the winter hemisphere, which are insignificant in case 2. This difference probably results from the different vertical shears in zonal wind between the two cases. Moreover, the region with negative \bar{q}_ϕ in the summer stratosphere polar region is also slightly more expansive in case 1. Correspondingly, the positive EP flux divergence for W3, which is an indication of wave source, is stronger in both the summer mesosphere polar region and the winter mesopause region for case 1. The positive EP flux divergence near the polar region of summer mesosphere is suggested to be evidence of wave amplification from the baroclinic/barotropic unstable region [Liu *et al.*, 2004]. The additional source for the W3 is evident from the positive EP flux divergence by the southward edge of the baroclinic/barotropic instability in the winter mesopause region for case 1 (Figure 7b).

Case 1 (Figures 7a and 7b) and case 3 (Figures 7e and 7f) are now compared. The stratospheric westerlies in the winter hemisphere polar region reverse to easterlies in case 3, which creates an area with negative \bar{q}_ϕ in the winter polar mesosphere and stratopause, compared with case 1 (Figures 7a and 7e). The additional W3 sources between 60°N and 90°N below 70 km in case 3 may be related to the nearby



301 instability (Figures 7b and 7f). It is also seen that the summer easterly winds in case 3
302 are stronger than in case 2 and case 1, which results in a larger refractive index for the
303 propagation of W3. The EP flux vectors in all the experimental runs show that the W3
304 propagates mainly southward from the northern hemisphere wave source region at
305 lower altitudes, and then propagates upward after reaching the southern hemisphere.
306 These propagation features agree well with previous model simulations [*Chang et al.*,
307 2011; *Yue et al.*, 2012].

308 The meridional and vertical components of the W3 EP flux (EPY and EPZ) are
309 shown in Figure 8. It is clear that both the EPY and EPZ are the strongest in case 1,
310 which is probably due to the energy transfer to child waves during the nonlinear
311 interaction between W3 and SPW1 for cases 2 and 3. In the northern (winter)
312 hemisphere, the stronger EPY and EPZ in case 1 may also be induced by the
313 additional northern mesospheric barotropic/baroclinic instabilities (shown in Figure
314 7a), which is not found in case 2 and case 3. The EPY components for all three cases
315 indicate southward propagation at lower altitudes from the wave source region in the
316 winter hemisphere, and then northward propagation in the summer polar mesosphere
317 near the region of instability. The EPZ mostly propagates upward, and is the strongest
318 at middle and low latitudes in the summer hemisphere and much weaker in the winter
319 hemisphere. This is in general agreement with the waveguide shown in Figure 7.
320 Strong upward EPZ at $\sim 30^\circ\text{N}$ and ~ 100 km is only observed in case 1, which is
321 probably related to the instability at middle and high latitudes (Figure 7a). Such
322 instabilities and wave sources disappear in the SSW runs due to the deceleration or



323 even reversal of the strong winter westerly winds.

324 Our simulations show that the instabilities at middle and high latitudes in the
325 winter hemisphere mesopause region can also provide additional and significant
326 sources for the amplification of W3 (case 1). Such instabilities and the corresponding
327 sources for W3 are weakened during SSW periods due to the deceleration or even
328 reversal of the winter stratospheric westerly winds. Our results also show that the
329 summer easterlies in the stratosphere and lower mesosphere are strengthened during
330 SSW periods, which results in larger waveguide and thus more favorable background
331 condition for the propagation of W3. The fact that W3 becomes weaker in the
332 presence of more favorable propagation conditions (and with the same wave source)
333 in the summer hemisphere again suggests a loss of W3 wave energy. In the following
334 section, we argue that the wave energy is transferred to child waves from nonlinear
335 interaction of W3 with SPW1, namely the QTDW W2 component.

336 **4.3 Nonlinear interaction between W3 and SPW1**

337 Figure 9a shows the wavenumber-period spectrum of the meridional wind during
338 model days 15-20 in case 3 at 100 km and 2.5°N. A westward wavenumber 2 QTDW
339 dominates the spectrum, which is different from the wavenumber 3 QTDW signature
340 shown in Figure 5a. The spectra of other components, e.g., zonal wind and
341 temperature, also show evident wavenumber 2 QTDW signatures. We should
342 emphasize that W3 and SPW1 are the only planetary waves specified at the lower
343 boundary of the TIME-GCM and no W2 signals are detected in the TIME-GCM runs
344 with only W3 or SPW1 perturbations imposed at the lower boundary (case 1 and case



345 4). Thus, the W2 in case 2 and case 3 is generated by the nonlinear interaction
346 between W3 and SPW1. The nonlinear interactions between two planetary waves can
347 generate two child waves with frequencies and zonal wavenumbers being the sum and
348 difference of the two parent waves [Teitelbaum and Vial, 1991]. For the nonlinear
349 interactions between W3 and SPW1, the frequencies (f , cycles per day) and zonal
350 wavenumbers (s) of the parents waves are: $(f, s) = (0.5, 3)$ and $(0, 1)$. Note here
351 positive (negative) s indicates a westward (eastward) propagating wave. Thus the
352 child waves are: $(f, s) = (0.5, 4)$ and $(0.5, 2)$. However, the wavenumber 4 QTDW is
353 not well resolved in our simulation due to its lower phase speed and larger dissipation
354 rate.

355 Figure 9b shows the cross section of the W2 in meridional wind for case 3 during
356 model days 15-20. It maximizes in the equatorial and low latitude regions at ~ 100 km
357 with a maximum amplitude of ~ 50 m/s. Shown in Figure 9c is the structure of the W2
358 in zonal wind and it peaks at middle latitudes with an amplitude nearly half as strong
359 as the meridional wind. Figure 9d shows the global structure of the W2 in temperature,
360 which exhibits similar global distributions as zonal wind. The temperature
361 perturbations show maximum amplitudes of ~ 10 K in both hemispheres at ~ 105 km,
362 and secondary maxima at ~ 85 km: ~ 7 K in the southern hemisphere and ~ 5 K in the
363 northern hemisphere. Figures 10a and 10b show the temporal variations of the W2 in
364 meridional wind at 100 km for case 2 and case 3, respectively. The perturbations of
365 the W2 in case 2 are weaker than in case 3, with maximum meridional wind
366 amplitudes of ~ 35 m/s and ~ 55 m/s, respectively. This increase in the W2 amplitude



367 in case 3 is consistent with the nonlinear interaction mechanism since one of the
368 parent waves (SPW1) is stronger in case 3, resulting in a stronger child wave.

369 The mean flow instabilities, the waveguide and the EP flux of W2 are also
370 examined to study the wave propagation and amplification. Figures 11a and 11c show
371 the zonal mean zonal wind during model days 15-20, when the W2 reaches the
372 strongest amplitude, for case 2 and case 3, respectively. In the northern hemisphere,
373 the mesospheric winter westerlies in case 3 are reversed in the polar region (Figure
374 11c), resulting in strong instabilities in this region. Weak instabilities are observed at
375 high latitudes in the winter mesopause region for case 2. In the southern hemisphere,
376 the summer easterly jet core at middle latitudes is stronger in case 3, which results in
377 a larger waveguide and thus more favorable condition for the propagation of W2 [*Liu*
378 *et al.*, 2004]. The mean flow instabilities in the summer polar region are similar
379 between case 2 and case 3.

380 Figures 11b and 11d show the EP flux of W2 and its divergence for case 2 and case 3,
381 respectively. The EP flux vectors show that W2 propagates in both summer and winter
382 hemispheres with comparable strength, which accounts for the nearly symmetric
383 global distribution of the wave perturbations (Figure 9). The propagation features of
384 W2 are different from W3 on that the W3 is more favorable to propagate in the
385 summer hemisphere (Figure 7). This is mainly due to the relatively larger phase speed
386 of W2, which results in a wider latitudinal distribution of positive waveguide for W2
387 and makes W2 less vulnerable to dissipation and critical layer filtering when
388 propagating upward in the winter hemisphere [*Salby and Callaghan*, 2001]. Positive



389 EP flux divergence is seen between 60 and 80 km at middle and high latitudes of the
390 summer hemisphere for both case 2 and case 3, which is probably due to the wave
391 amplification by the nearby region of instability [Liu *et al.*, 2004]. In addition, large
392 positive EP flux divergence regions are found at middle and high latitudes of the
393 northern hemisphere between 50-100 km for both case 2 and case 3, which is an
394 indication of wave source due to the nonlinear interaction between SPW1 and W3. In
395 addition, the positive EP flux divergence of W3 between 30°N and 60°N below 80 km
396 (Figure 11d) may be related to the negative \bar{q}_ϕ in the winter polar stratosphere (Figure
397 11c). Figure 12 shows the meridional and vertical components (EPY and EPZ) of the
398 EP flux of W2 separately. Both the EPY and EPZ are stronger in case 3 than case 2,
399 which is again consistent with the nonlinear interaction mechanism. The vertical
400 component EPZ (Figures 12b and 12d) clearly shows that the W2 propagates upward
401 nearly symmetrically in both summer and winter hemispheres.

402 Figures 13a and 13b show the EP fluxes of W3 and SPW1 during model days
403 15-20 in case 3. Strong upward propagating SPW1 from wave source region is seen at
404 middle and high latitudes in the winter hemisphere. Meanwhile, the energy of W3
405 propagates mainly southward from the same wave source region. Thus the nonlinear
406 coupling between SPW1 and W3 is most likely to occur at lower altitudes in the
407 winter hemisphere near the wave source region. In addition, weaker W3 energy can
408 also be identified at higher altitudes and at middle and low latitudes in the winter
409 hemisphere, which, together with the strong SPW1 energy at the same region, could
410 also contribute to the source of W2 through nonlinear coupling. These speculations



are further investigated by calculating the nonlinear advective tendency between W3 and SPW1. The nonlinear advective tendency terms in the momentum equations, which have been utilized by *Chang et al.* [2011] in studying the nonlinear coupling between QTDW and tides, are of the form:

$$\vec{F}_{advective} = -\vec{V} \cdot \nabla V = -\left\{ \frac{u}{a \cos \varphi} \frac{\partial}{\partial \lambda} + \frac{v}{a} \frac{\partial}{\partial \varphi} + w \frac{\partial}{\partial z} \right\} \begin{bmatrix} u \\ v \end{bmatrix}^T \quad (4)$$

Where u , v and w are the zonal, meridional and vertical winds, a , z , φ and λ are the earth radius, altitude, latitude, and longitude. By decomposing wind components, including zonal, meridional and vertical winds, into the forms of $r \approx \bar{r} + r_1 + r_2$ (\bar{r} , r_1 and r_2 represent the zonal mean wind and the wind perturbations of the two planetary waves, respectively), the zonal and meridional components of the nonlinear coupling tendencies for two planetary waves are:

$$\vec{F}_{nonlinear,x} = -\frac{1}{a \cos \varphi} (u_1 \frac{\partial u_2}{\partial \lambda} + u_2 \frac{\partial u_1}{\partial \lambda}) - \frac{1}{a} (v_1 \frac{\partial u_2}{\partial \varphi} + v_2 \frac{\partial u_1}{\partial \varphi}) - (w_1 \frac{\partial u_2}{\partial z} + w_2 \frac{\partial u_1}{\partial z}) \quad (5)$$

$$\vec{F}_{nonlinear,y} = -\frac{1}{a \cos \varphi} (u_1 \frac{\partial v_2}{\partial \lambda} + u_2 \frac{\partial v_1}{\partial \lambda}) - \frac{1}{a} (v_1 \frac{\partial v_2}{\partial \varphi} + v_2 \frac{\partial v_1}{\partial \varphi}) - (w_1 \frac{\partial v_2}{\partial z} + w_2 \frac{\partial v_1}{\partial z}) \quad (6)$$

where \bar{u} , \bar{v} and \bar{w} are the zonal mean zonal, meridional and vertical winds, u_1 and u_2 , v_1 and v_2 , w_1 and w_2 are the zonal, meridional, vertical wind perturbations for two different planetary waves. By adopting a complex perturbation of the form $u' = \hat{u} e^{i(\sigma t - s \lambda)}$ (the σ and s are the frequency and zonal wavenumber of the planetary wave, t is the universal time), the complex amplitudes of the nonlinear advective tendencies can be calculated as:

$$\vec{F}_{nonlinear,x} = \frac{i \hat{u}_1 \hat{u}_2}{a \cos \varphi} (s_1 + s_2) - \frac{1}{a} (\hat{v}_1 \frac{\partial \hat{u}_2}{\partial \varphi} + \hat{v}_2 \frac{\partial \hat{u}_1}{\partial \varphi}) - (\hat{w}_1 \frac{\partial \hat{u}_2}{\partial z} + \hat{w}_2 \frac{\partial \hat{u}_1}{\partial z}) \quad (7)$$



$$\vec{F}_{nonlinear,y} = \frac{i}{a \cos \varphi} (\hat{u}_1 \hat{v}_2 s_2 + \hat{u}_2 \hat{v}_1 s_1) - \frac{1}{a} (\hat{v}_1 \frac{\partial \hat{v}_2}{\partial \varphi} + \hat{v}_2 \frac{\partial \hat{v}_1}{\partial \varphi}) - (\hat{w}_1 \frac{\partial \hat{v}_2}{\partial z} + \hat{w}_2 \frac{\partial \hat{v}_1}{\partial z}) \quad (8)$$

where s_1 and s_2 are the zonal wavenumbers of different planetary waves, \hat{u}_1 and \hat{u}_2 , \hat{v}_1 and \hat{v}_2 , \hat{w}_1 and \hat{w}_2 are the zonal, meridional, vertical wind amplitudes for two different planetary waves.

Figure 13c shows the amplitude of the meridional component of the nonlinear advective tendency between W3 and SPW1 (equation 8). The nonlinear coupling between W3 and SPW1 maximizes at lower altitudes in the northern hemisphere, which is not surprising since both the W3 and SPW1 perturbations are forced at the lower model boundary in the northern hemisphere. Correspondingly, a strong W2 source is present at lower altitudes in the northern hemisphere, which is also suggested by the positive EP flux divergence shown in Figure 11d. The large nonlinear advection value at the lower boundary is due to the large wave sources forced there to compensate for the unrealistic wave decay usually found near the model lower boundary. Although the amplitude of the advective tendency at the lower model boundary may be too large, it is still likely that the nonlinear interaction between W3 and SPW1 at ~10 hPa in the winter hemisphere is strong, since climatologically the sources of W3 and SPW1 are found to maximize in the winter hemisphere at stratospheric heights. There is an additional region extending from 60 km to about 100 km at low to mid latitudes where the advective tendency term becomes significant (with a peak at ~70km). This is again consistent with the positive EP flux divergence in Figure 11d, and is likely due to the nonlinear coupling of W3 and SPW1.



453 5. Conclusions

454 The influence of the SSW on the QTDW was investigated with NCAR
455 TIME-GCM simulations. The westward wavenumber 3 QTDW was simulated by
456 specifying geopotential height perturbations of 1000 m at the lower model boundary
457 (~30 km) for both the standard W3 run and the SSW runs. Wavenumber 1 stationary
458 planetary waves with geopotential height perturbations of 1000 m and 2800 m were
459 forced in the northern hemisphere at the lower model boundary to induce minor and
460 major SSWs, respectively.

461 We find that the mean flow instabilities at middle and high latitudes in the winter
462 mesopause region can provide additional and essential sources for the amplification of
463 W3, whereas such instabilities are weakened during SSW periods due to the
464 deceleration or even reversal of the winter westerlies. The mean flow instabilities in
465 the winter stratosphere polar region, induced by the mean wind reversal from westerly
466 to easterly during SSW periods may also contribute to the amplification of W3. The
467 waveguide of the W3 is larger during SSW periods, which favors the propagation of
468 W3. The wave energy of W3 could be transmitted to child waves through the
469 nonlinear interaction between W3 and stationary planetary waves during the SSW
470 periods.

471 The nonlinear interaction between W3 and the SPW1 results in a new kind of
472 westward QTDW with zonal wavenumber 2. The W2 is generated mainly in the wave
473 source region, and then propagates into both summer and winter hemispheres. The
474 meridional wind perturbations of W2 maximize in the equatorial region, whereas the



475 zonal wind and temperature components peak at middle latitudes. The EP flux
476 diagnostics show that W2 is capable of propagating in both hemispheres, which
477 results in much more symmetric global structures than W3 for both wind and
478 temperature components. This is probably due to the larger phase speed of W2, which
479 results in larger latitudinal distributions of positive waveguide and makes W2 less
480 vulnerable to dissipation and critical layer filtering by the background wind when
481 propagating upward. In the summer hemisphere, the instabilities in the upper
482 stratosphere and lower mesosphere polar region may contribute to the amplification of
483 W2 through wave-mean flow interaction. In the winter hemisphere, the nonlinear
484 coupling between W3 and SPW1 at middle and low latitudes between 50 km and 100
485 km, and the instabilities induced by the reversal of winter stratosphere westerly during
486 SSW periods, most probably provide additional sources for W2. The stronger
487 stationary planetary wave accounts for the stronger W2 perturbations during major
488 SSW period by transmitting more energy to W2 during the nonlinear interaction
489 between W3 and SPW1. Moreover, the background mean flow condition is also more
490 favorable for the propagation of W2 during major SSW period with a larger
491 waveguide. We should note that the amplitudes of W3 and SPW1 specified at the
492 lower boundary were both set to constant values in our simulation, while the wave
493 sources would vary with time in real atmosphere. In the future, we plan to use more
494 realistic assimilation datasets (e.g., ECMWF) as the lower model boundary to further
495 study the influence of SSW on QTDWs, to understand the variability of the wave
496 sources, and their possible relation with SSW.



497

498 **Acknowledgements**

499 This work is funded by the Project Supported by the Specialized Research Fund for
500 State Key Laboratories, the Project Funded by China Postdoctoral Science Foundation,
501 the National Natural Science Foundation of China (41274150, 41421063), the
502 Chinese Academy of Sciences Key Research Program (KZZD-EW-01-1), the National
503 Basic Research Program of China (2012CB825605). The data utilized in this paper is
504 from TIME-GCM simulations on NCAR Yellowstone computing system
505 (ark:/85065/d7wd3xhc), sponsored by the National Science Foundation. H.L.
506 acknowledges support from NSF grant AGS-1138784.



507 **Reference**

- 508 Andrews, D. G., J. R. Holton, and C. B. Leovy (1987), Middle Atmosphere Dynamics,
509 489 pp., Academic, San Diego, Calif.
- 510 Burks, D., and C. Leovy (1986), Planetary waves near the mesospheric easterly jet,
511 *Geophys. Res. Lett.*, *13*, 193-196, doi: 10.1029/GL013i003p00193.
- 512 Chandran, A., R. R. Garcia, R. L. Collins, and L. C. Chang (2013), Secondary
513 planetary waves in the middle and upper atmosphere following the stratospheric
514 sudden warming event of January 2012, *Geophys. Res. Lett.*, *40*, 1861–1867,
515 doi:10.1002/grl.50373.
- 516 Chang, L. C., S. E. Palo, and H. L. Liu (2011), Short-term variability in the migrating
517 diurnal tide caused by interactions with the quasi 2 day wave, *J. Geophys. Res.*,
518 *116*, D12112, doi:10.1029/2010JD014996.
- 519 Funke, B., M. López-Puertas, D. Bermejo-Pantaleón, M. García-Comas, G. P. Stiller,
520 T. von Clarmann, M. Kiefer, and A. Linden (2010), Evidence for dynamical
521 coupling from the lower atmosphere to the thermosphere during a major
522 stratospheric warming, *Geophys. Res. Lett.*, *37*, L13803,
523 doi:10.1029/2010GL043619.
- 524 Gu, S. Y., T. Li, X. K. Dou, Q. Wu, M. G. Mlynczak, and J. M. Russell (2013a),
525 Observations of Quasi-Two-Day wave by TIMED/SABER and TIMED/TIDI, *J.*
526 *Geophys. Res. Atmos.*, *118*, 1624–1639, doi:10.1002/jgrd.50191.
- 527 Gu, S. Y., T. Li, X. Dou, N.-N. Wang, D. Riggin, and D. Fritts (2013b), Long-term
528 observations of the quasi two-day wave by Hawaii MF radar, *J. Geophys. Res.*



- 529 *Space Physics*, 118, 7886–7894, doi:10.1002/2013JA018858.
- 530 Harada, Y., A. Goto, H. Hasegawa, N. Fujikawa, H. Naoe, and T. Hirooka (2009), A
 531 Major Stratospheric Sudden Warming Event in January 2009, *J. Atmos. Sci.*, 67,
 532 2052-2069, doi:http://dx.doi.org/10.1175/2009JAS3320.1.
- 533 Heelis, R. A., J. K. Lowell, and R. W. Spiro (1982), A model of the high-latitude
 534 ionosphere convection pattern, *J. Geophys. Res.*, 87, 6339–6345.
- 535 Karlsson, B., H. Kørnich, and J. Gumbel (2007), Evidence for interhemispheric
 536 stratosphere-mesosphere coupling derived from noctilucent cloud properties,
 537 *Geophys. Res. Lett.*, 34, L16806, doi:10.1029/2007GL030282.
- 538 Karlsson, B., C. McLandress, and T. G. Shepherd (2009), Inter-hemispheric
 539 mesospheric coupling in a comprehensive middle atmosphere model, *J. Atmos.*
 540 *Sol. Terr. Phys.*, 71, 518-530, doi:10.1016/j.jastp.2008.08.006.
- 541 Limpasuvan, V., and D. L. Wu (2009), Anomalous two-day wave behavior during the
 542 2006 austral summer, *Geophys. Res. Lett.*, 36, L04807,
 543 doi:10.1029/2008GL036387.
- 544 Limpasuvan, V., C. B. Leovy, and Y. J. Orsolini (2000), Observed temperature
 545 two-day wave and its relatives near the stratopause, *J. Atmos. Sci.*, 57, 1689-1701,
 546 doi:10.1175/1520-0469(2000)057%3C1689:OTTDWA%3E2.0.CO;2.
- 547 Lindzen, R. S. (1981), Turbulence and Stress Owing to Gravity Wave and Tidal
 548 Breakdown, *J. Geophys. Res.*, 86, 9707-9714, doi:10.1029/JC086iC10p09707.
- 549 Liu, H. L., E. R. Talaat, R. G. Roble, R. S. Lieberman, D. M. Riggan, and J. H. Yee
 550 (2004), The 6.5-day wave and its seasonal variability in the middle and upper



- 551 atmosphere, *J. Geophys. Res.*, *109*, D21112, doi:10.1029/2004JD004795.
- 552 Liu, H. L., and A. D. Richmond (2013), Attribution of ionospheric vertical plasma
 553 drift perturbations to large-scale waves and the dependence on solar activity, *J.*
 554 *Geophys. Res.*, *118*, 2452-2465, doi:10.1002/jgra.50265.
- 555 Liu, H. L., W. Wang, A. D. Richmond, and R. G. Roble (2010), Ionospheric variability
 556 due to planetary waves and tides for solar minimum conditions, *J. Geophys. Res.*,
 557 *115*, A00G01, doi:10.1029/2009JA015188.
- 558 Manney, G. L., et al. (2009), Satellite observations and modeling of transport in the
 559 upper troposphere through the lower mesosphere during the 2006 major
 560 stratospheric sudden warming, *Atmos Chem Phys*, *9*, 4775-4795,
 561 doi:10.5194/acp-9-4775-2009.
- 562 Matsuno, T. (1971), A Dynamical Model of the Stratospheric Sudden Warming, *J.*
 563 *Atmos. Sci.*, *28*, 1479-1494,
 564 doi:http://dx.doi.org/10.1175/1520-0469(1971)028<1479:ADMOTS>2.0.CO;2.
- 565 McCormack, J. P., L. Coy, and K. W. Hoppel (2009), Evolution of the quasi 2-day
 566 wave during January 2006, *J. Geophys. Res.*, *114*, D20115,
 567 doi:10.1029/2009JD012239.
- 568 Mertens, C. J., et al. (2009), Kinetic temperature and carbon dioxide from broadband
 569 infrared limb emission measurements taken from the TIMED/SABER instrument,
 570 *Adv. Space. Res.*, *43*, 15-27.
- 571 Palo, S. E., J. M. Forbes, X. Zhang, J. M. Russell, III, and M. G. Mlynczak (2007), An
 572 eastward propagating two-day wave: Evidence for nonlinear planetary wave and



- 573 tidal coupling in the mesosphere and lower thermosphere, *Geophys. Res. Lett.*,
 574 34, L07807, doi:10.1029/2006GL027728.
- 575 Pancheva, D., et al. (2008), Latitudinal wave coupling of the stratosphere and
 576 mesosphere during the major stratospheric warming in 2003/2004, *Ann.*
 577 *Geophys.*, 26, 467-483, doi:10.5194/angeo-26-467-2008.
- 578
- 579 Plumb, R. A. (1983), Baroclinic Instability of the Summer Mesosphere: A Mechanism
 580 for the Quasi-Two-Day Wave?, *J. Atmos. Sci.*, 40(1), 262-270,
 581 doi:10.1175/1520-0469(1983)040<0262:BIOTSM>2.0.CO;2.
- 582 Richmond, A. D., E. C. Ridley, and R. G. Roble (1992), A thermosphere/ionosphere
 583 general circulation model with coupled electrodynamics, *Geophys. Res. Lett.*, 19,
 584 601–604.
- 585 Riggins, D. M., R. S. Lieberman, R. A. Vincent, A. H. Manson, C. E. Meek, T.
 586 Nakamura, T. Tsuda, and Y. I. Portnyagin (2004), The 2-day wave during the
 587 boreal summer of 1994, *J. Geophys. Res.*, 109, D08110,
 588 doi:10.1029/2003JD004493.
- 589 Roble, R. G. (2000), On the feasibility of developing a global atmospheric model
 590 extending from the ground to the exosphere, in *Atmospheric Science Across the*
 591 *Stratopause*, edited by D. E. Siskind, S. D. Eckermann, and M. E. Summers, 342
 592 p., no. 123 in Geophysical Monograph Series, American Geophysical Union,
 593 Washington, D.C.
- 594 Roble, R. G., and E. C. Ridley (1987), An auroral model for the NCAR thermosphere



- 595 general circulation model (TGCM), *Annales. Geophysicae.*, *5A*, 369–382.
- 596 Roble, R. G., and E. C. Ridley (1994), A
- 597 thermosphere-ionosphere-mesosphere-electrodynamics general circulation model
- 598 (time-GCM): Equinox solar cycle minimum simulations (30–500 km), *Geophys.*
- 599 *Res. Lett.*, *21*, 417-420, doi:10.1029/93GL03391.
- 600 Rodgers, C. D., and A. J. Prata (1981), Evidence for a Traveling 2-Day Wave in the
- 601 Middle Atmosphere, *J. Geophys. Res.*, *86*, 9661-9664,
- 602 doi:10.1029/JC086iC10p09661.
- 603 Rojas, M., and W. Norton (2007), Amplification of the 2-day wave from mutual
- 604 interaction of global Rossby-gravity and local modes in the summer mesosphere,
- 605 *J. Geophys. Res.*, *112*, D12114, doi:10.1029/2006JD008084.
- 606 Salby, M. L. (1981), The 2-Day Wave in the Middle Atmosphere: Observations and
- 607 Theory, *J. Geophys. Res.*, *86*, 9654-9660, doi:10.1029/JC086iC10p09654.
- 608 Salby, M. L., and P. F. Callaghan (2001), Seasonal Amplification of the 2-Day Wave:
- 609 Relationship between Normal Mode and Instability, *J. Atmos. Sci.*, *58*(14),
- 610 1858-1869,
- 611 doi:10.1175/1520-0469(2001)058%3C1858:SAOTDW%3E2.0.CO;2.
- 612
- 613 Swinbank, R., and D. A. Ortland (2003), Compilation of wind data for the Upper
- 614 Atmosphere Research Satellite (UARS) Reference Atmosphere Project, *J.*
- 615 *Geophys. Res.*, *108*, 4615.
- 616 Tan, B., X. Chu, H.-L. Liu, C. Yamashita, and J. M. Russell, III (2012), Zonal-mean



- 617 global teleconnection from 15 to 110 km derived from SABER and WACCM, *J.*
 618 *Geophys. Res.*, *117*, D10106, doi:10.1029/2011JD016750.
- 619 Teitelbaum, H., and F. Vial (1991), On Tidal Variability Induced by
 620 Nonlinear-Interaction with Planetary-Waves, *J Geophys Res.*, *96*, 14169-14178,
 621 doi:10.1029/91JA01019.
- 622 Tunbridge, V. M., D. J. Sandford, and N. J. Mitchell (2011), Zonal wave numbers of
 623 the summertime 2 day planetary wave observed in the mesosphere by EOS Aura
 624 Microwave Limb Sounder, *J. Geophys. Res.*, *116*, D11103,
 625 doi:10.1029/2010jd014567.
- 626 Wu, D. L., E. F. Fishbein, W. G. Read, and J. W. Waters (1996), Excitation and
 627 Evolution of the Quasi-2-Day Wave Observed in UARS/MLS Temperature
 628 Measurements, *Journal of the Atmospheric Sciences*, *53*, 728-738,
 629 doi:10.1175/1520-0469(1996)053<0728:EAEOTQ>2.0.CO;2.
- 630 Wu, D. L., P. B. Hays, W. R. Skinner, A. R. Marshall, M. D. Burrage, R. S. Lieberman,
 631 and D. A. Ortland (1993), Observations of the Quasi 2-Day Wave from the
 632 High-Resolution Doppler Imager on Uars, *Geophys. Res. Lett.*, *20*, 2853-2856,
 633 doi:10.1029/93GL03008.
- 634 Yamashita, C., H. -L. Liu, and X. Chu (2010), Responses of mesosphere and lower
 635 thermosphere temperatures to gravity wave forcing during stratospheric sudden
 636 warming, *Geophys. Res. Lett.*, *37*, L09803, doi:10.1029/2009GL042351.
- 637 Yue, J., H.-L. Liu, and L. C. Chang (2012), Numerical investigation of the quasi 2 day
 638 wave in the mesosphere and lower thermosphere, *J. Geophys. Res.*, *117*, D05111,



639 doi:10.1029/2011JD016574.

640



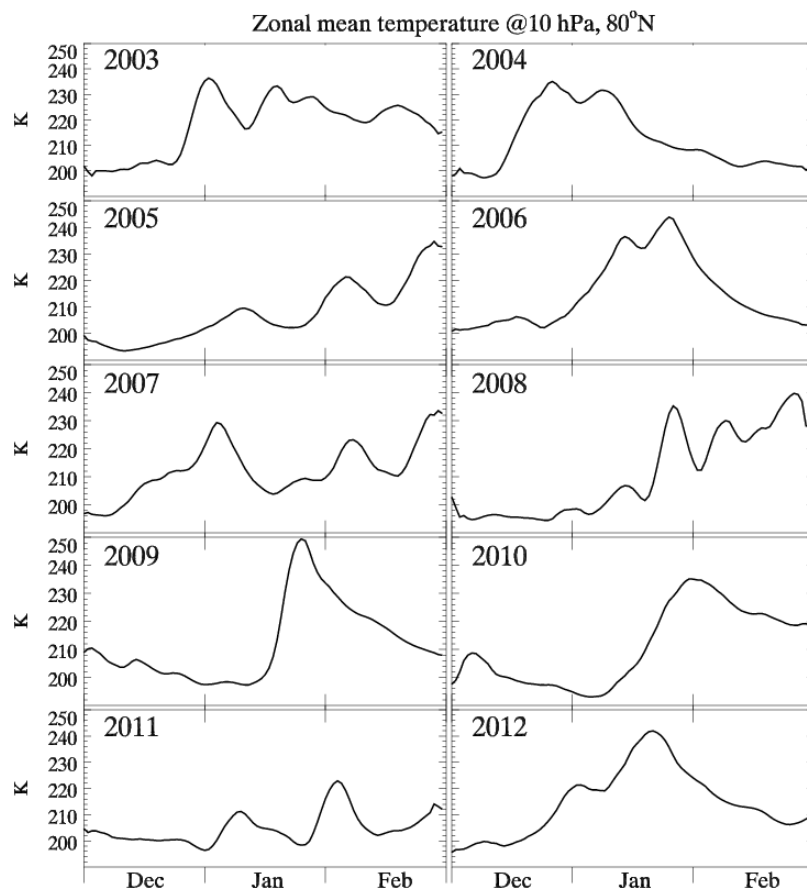
641

	GP Height of W3	GP Height of SPW1
Base case	×	×
Case 1	1000 m	×
Case 2	1000 m	1000 m
Case 3	1000 m	2800 m
Case 4	×	2800 m

642 **Table 1.** The geopotential height perturbations of W3 and SPW1 specified at the
 643 lower model boundary for different model runs.
 644
 645
 646
 647
 648



649



650

651

652

653

Figure 1. The ECMWF zonal mean temperature at 80°N and 10 hPa from December to February during 2003-2012.

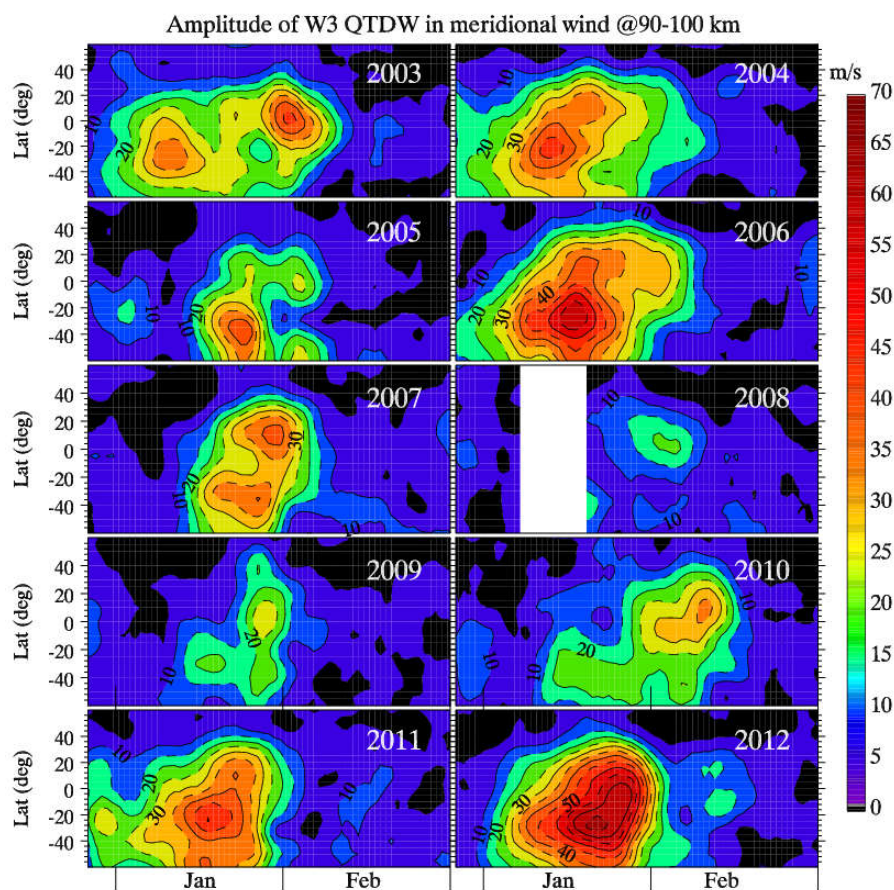


Figure 2. The temporal variations of the wave number 3 QTDW in January and February during 2003-2012. The amplitudes are averaged between 90 and 100 km.

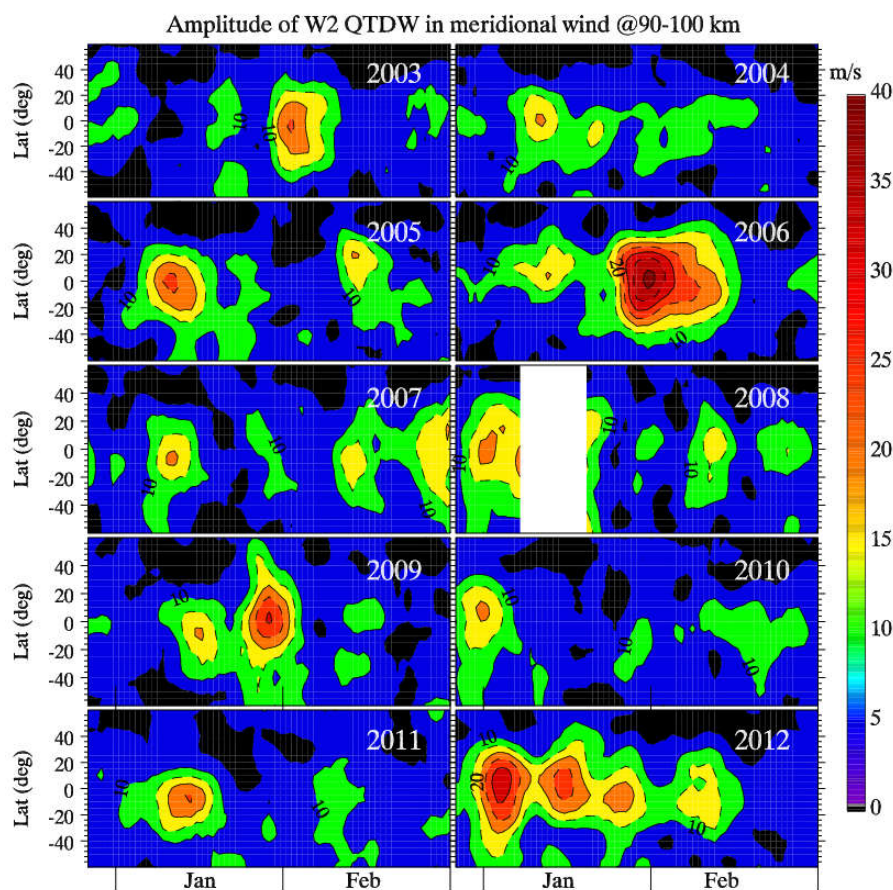


Figure 3. The same as Figure 2 but for the wave number 2 QTDW.

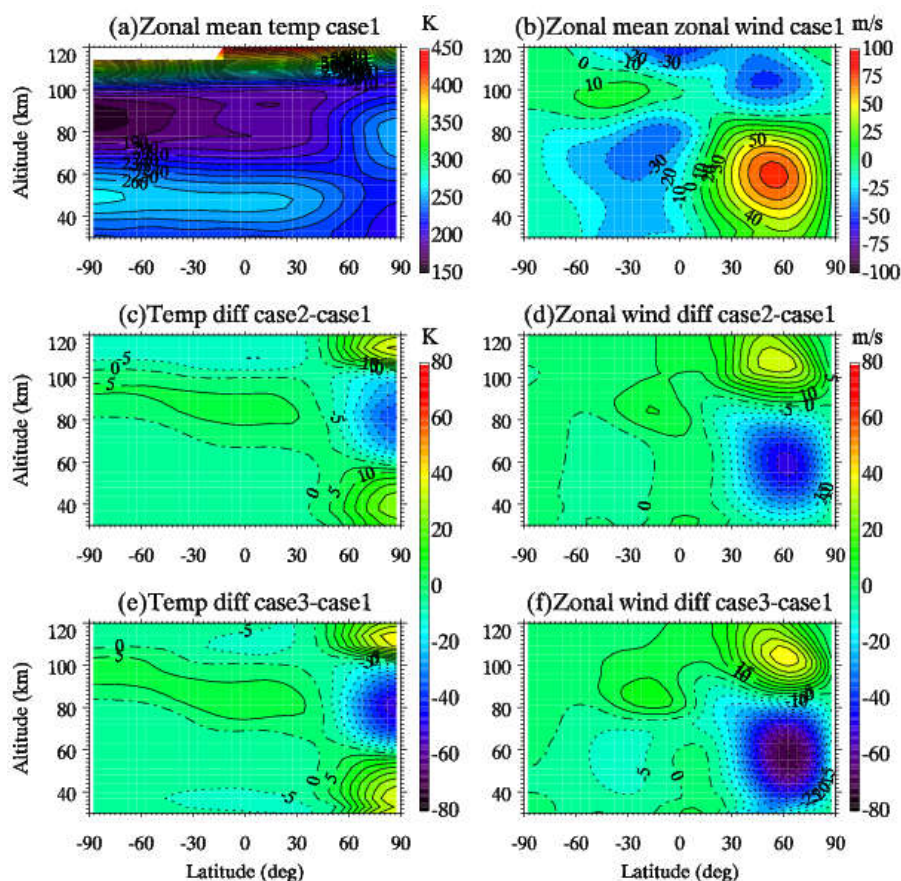


Figure 4. The zonal mean (a) temperature and (b) zonal wind in case 1 on model day 28. The temperature and zonal wind differences between (c, d) case 2 and case 1, (e, f) case 3 and case 1 are also shown. The temperature contour intervals are 10 K in (a) and 5 K in (c) and (e). The zonal wind contour intervals are 10 m/s in (b) and 5 m/s in (d) and (f).

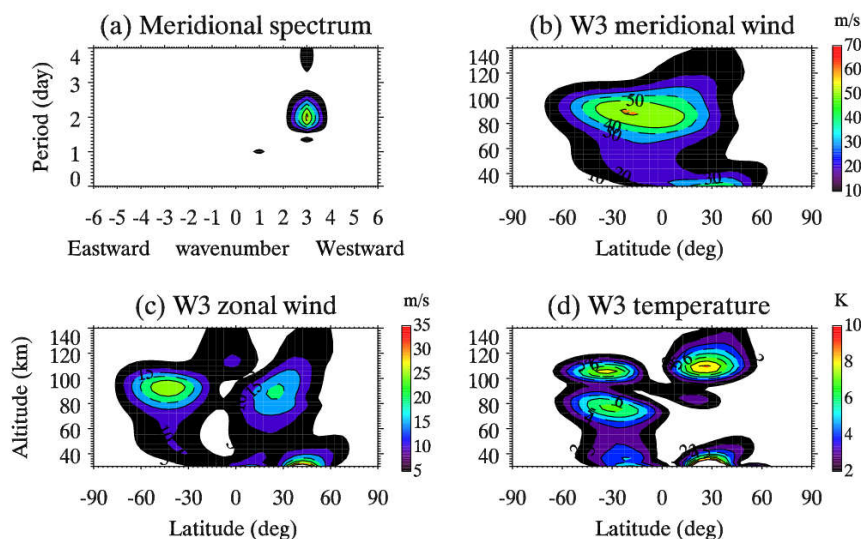
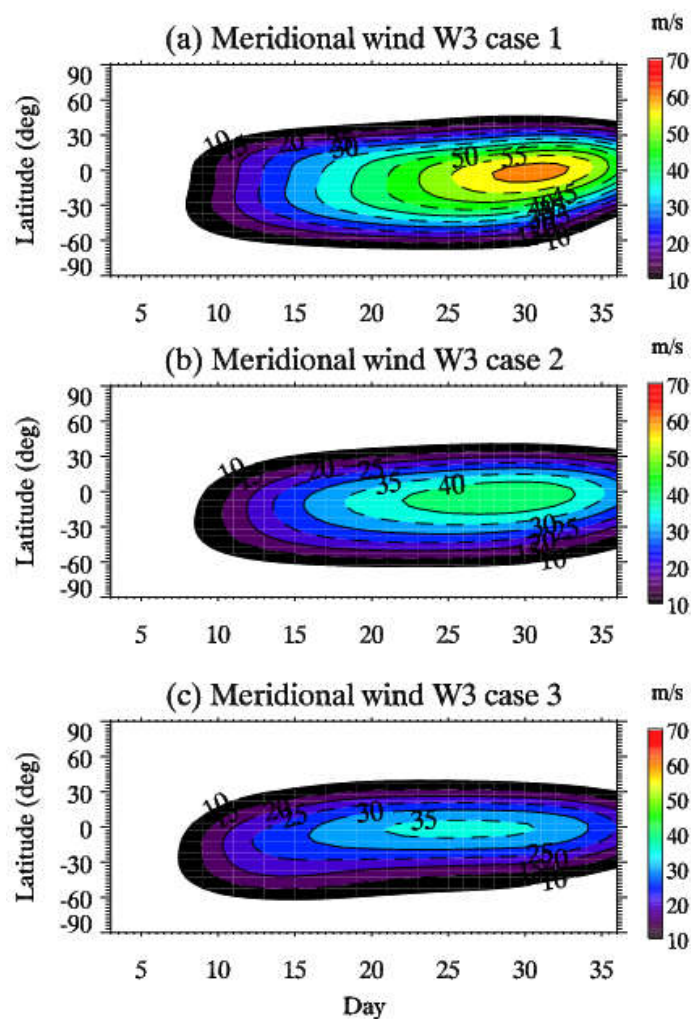


Figure 5. (a) The least-square fitting spectrum of the meridional wind at 22.5°S and ~90 km during model day 25-30 of case 1. A westward wave number 3 QTDW dominates the spectrum. The vertical and global structures of the W3 in meridional wind, zonal wind and temperature are shown in (b), (c) and (d), respectively. The contour intervals are 10 m/s, 5 m/s and 1 K for meridional wind, zonal wind and temperature, respectively.



676

677 **Figure 6.** The temporal variations of the W3 at 82 km for (a) case 1, (b) case 2 and (c)
 678 case 3. Geopotential height perturbations of 1000 m are forced at the lower boundary
 679 for all the three control runs to simulate the W3. SPW1 geopotential height
 680 perturbations of 1000 m and 2800 m are forced at the lower boundary to induce the
 681 weak and strong SSWs in case 2 and case 3, respectively. No SPW1 perturbations are
 682 forced at the lower boundary of case 1. The contour intervals are 5 m/s.
 683

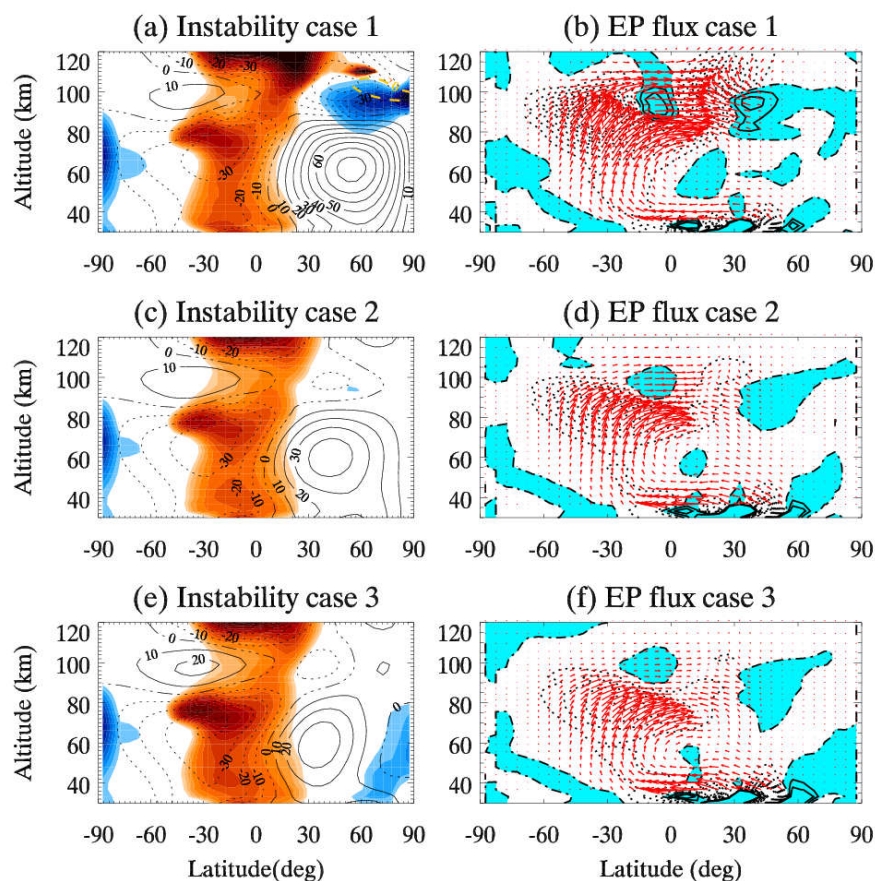


Figure 7. The zonal mean zonal wind during model days 25-30 for (a) case 1, (c) case 2 and (e) case 3. The baroclinic/barotropic instabilities are overplotted with blue shades. The orange shaded region denotes the positive (propagating) waveguide (m^2) for W3. Shown on the right are the EP flux vectors (red arrows) and their divergences (light blue shade for positive value, dot line for negative value) for (b) case 1, (d) case 2 and (f) case 3. The contour intervals for the EP flux divergence are 2 m/s/day.

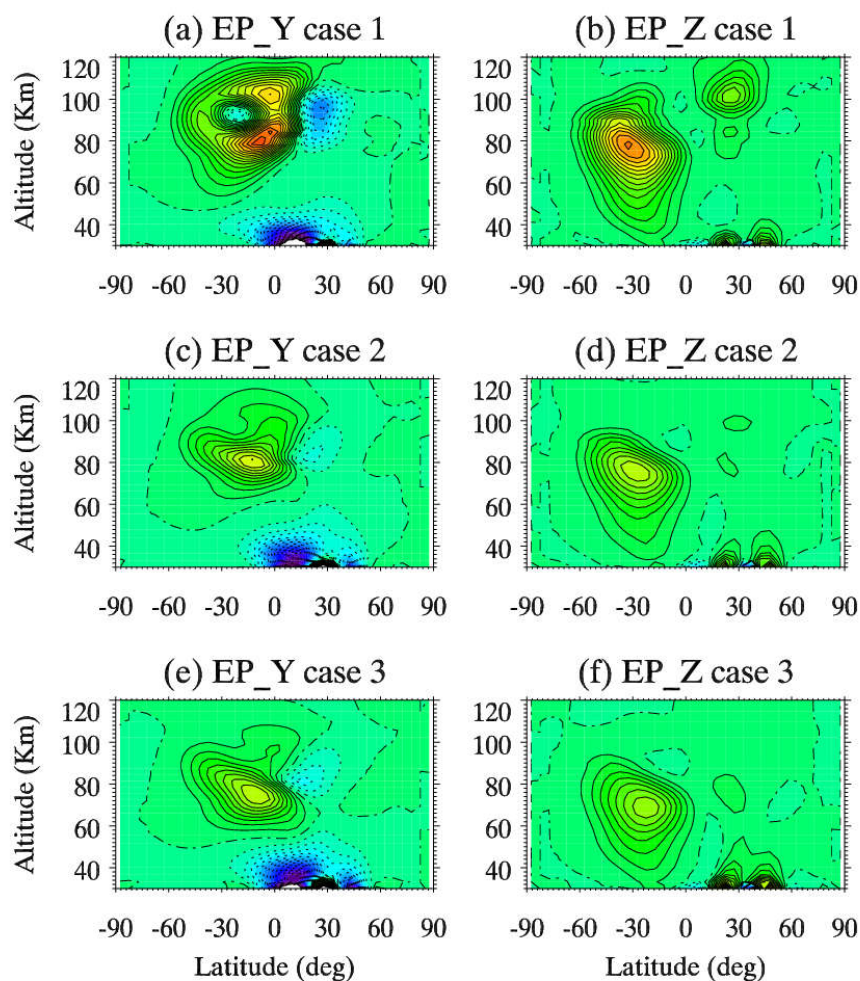


Figure 8. (left) Meridional and (right) vertical components of the EP flux of the W3 during model day 25-30 for (a, b) case 1, (c, d) case 2 and (e, f) case 3. The solid contours are for northward or upward directions. Both components have been normalized by the air density.

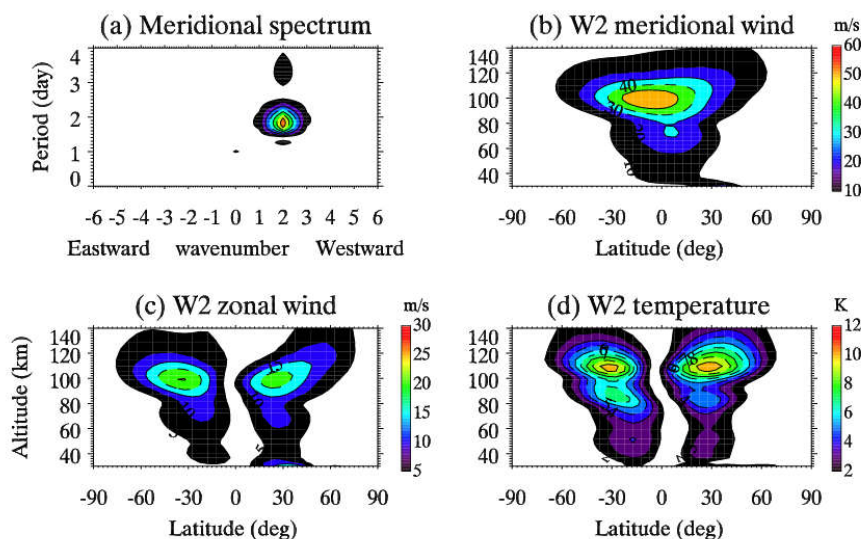


Figure 9. Similar to Figure 5 but for case 3 during model days 15-20. Figure 9a shows the meridional wind spectrum at 100 km and 2.5°N. Figures 9b, 9c and 9d show the global and vertical structures of W2 for meridional wind, zonal wind and temperature, respectively.

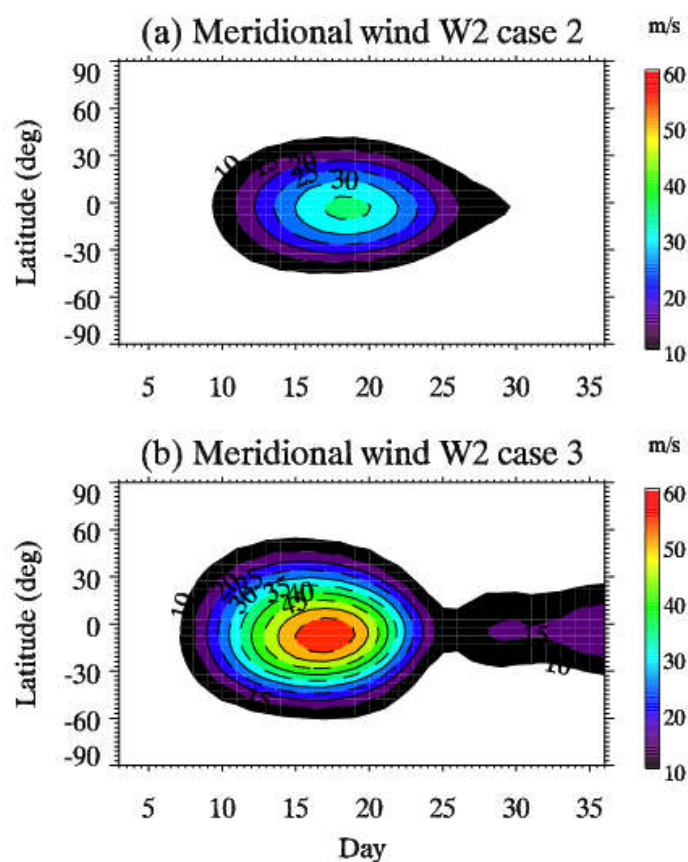


Figure 10. The temporal variations of the W2 at 100 km for (a) case 2 and (b) case 3.
 The contour intervals are 5 m/s.

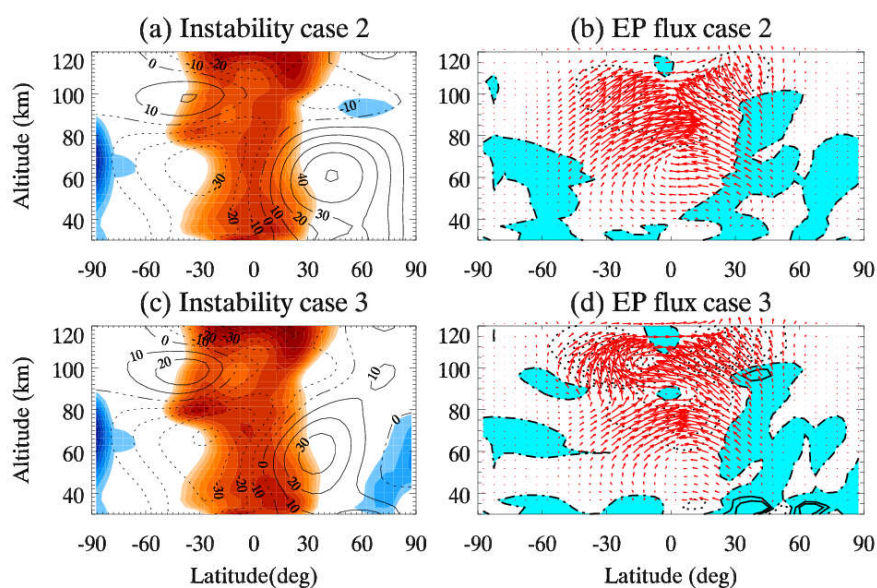


Figure 11. The same as Figure 7 but for the W2 during model day 15-20 for (a, b) case 2 and (c, d) case 3.

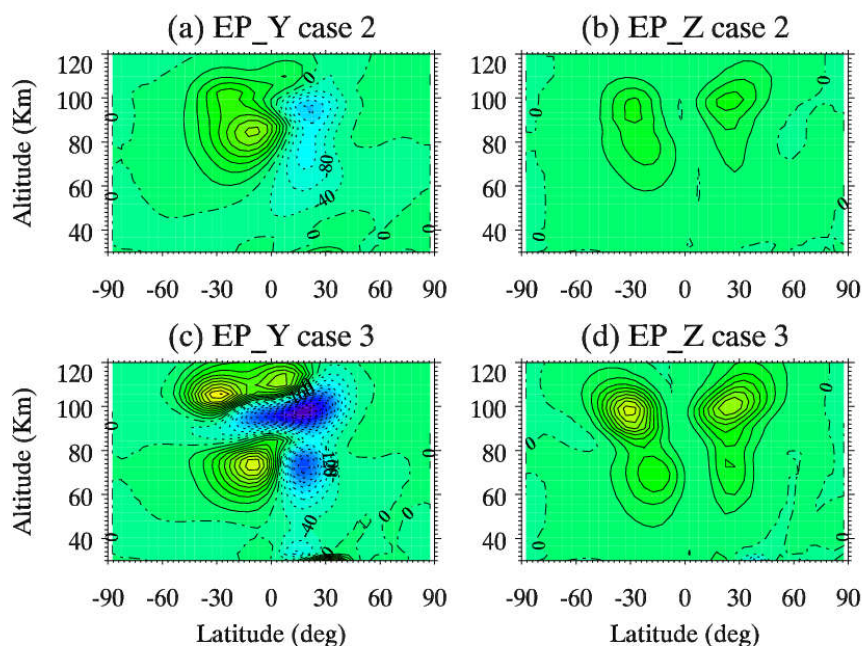


Figure 12. The same as Figure 8 but for the W2 during model day 15-20 for (a, b) case 2 and (c, d) case 3.

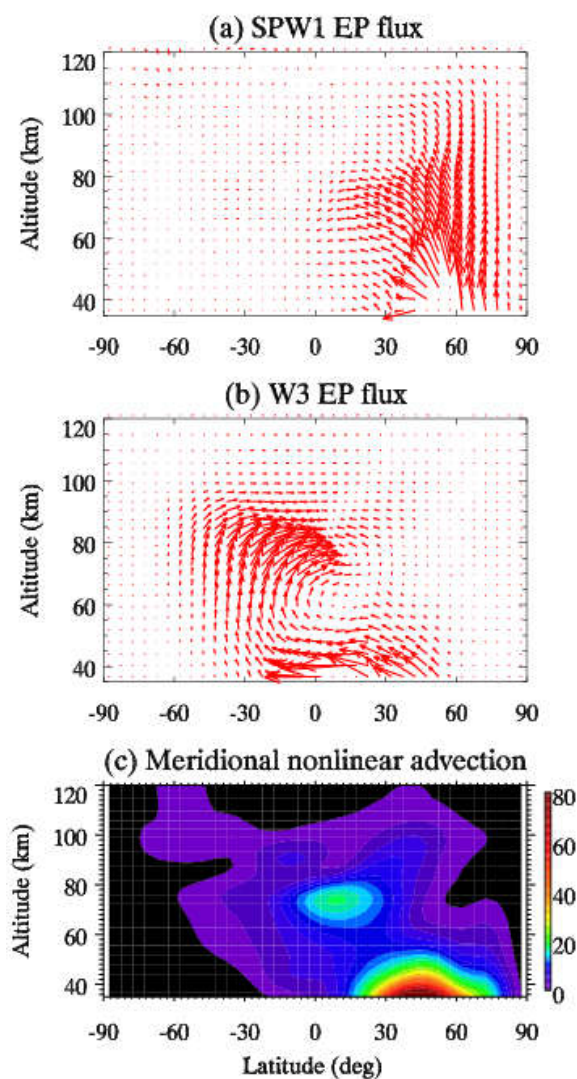


Figure 13. The EP flux vectors of (a) the SPW1 and (b) the W3 during model day 15-20 of case 3. (c) The amplitude (m/s^2) of the meridional component of the nonlinear advection tendency between W3 and SPW1.